



Open Archive Toulouse Archive Ouverte (OATAO)

OATAO is an open access repository that collects the work of Toulouse researchers and makes it freely available over the web where possible.

This is an author-deposited version published in: <http://oatao.univ-toulouse.fr/>
Eprints ID: 16158

To link to this article : DOI: 10.1016/j.pepi.2016.05.017

URL : <http://dx.doi.org/10.1016/j.pepi.2016.05.017>

To cite this version: Khan, Amir and van Driel, Martin and Böse, Maren and Giardini, Domenico and Ceylan, Savas and Yan, Jun and Clinton, John Francis and Euchner, Fabian and Lognonné, Philippe and Murdoch, Naomi and Mimoun, David and Panning, Mark and Knapmeyer, Martin and Banerdt, W. Bruce *Single-station and single-event marsquake location and inversion for structure using synthetic Martian waveforms*. (2016) Physics of the Earth and Planetary Interiors, vol. 258. pp. 28-42. ISSN 0031-9201

Single-station and single-event marsquake location and inversion for structure using synthetic Martian waveforms

A. Khan ^{a,*}, M. van Driel ^a, M. Böse ^{a,b}, D. Giardini ^a, S. Ceylan ^a, J. Yan ^a, J. Clinton ^b, F. Euchner ^a, P. Lognonné ^c, N. Murdoch ^d, D. Mimoun ^d, M. Panning ^e, M. Knapmeyer ^f, W.B. Banerdt ^g

^a Institute of Geophysics, ETH Zürich, Switzerland

^b Swiss Seismological Service, ETH Zürich, Switzerland

^c Institut de Physique du Globe de Paris, Paris, France

^d ISAE-SUPAERO, Université de Toulouse, DEOS/Systèmes Spatiaux, France

^e Department of Geological Sciences, University of Florida, Gainesville, USA

^f Institute for Planetary Research, DLR, Berlin, Germany

^g Jet Propulsion Laboratory, California Institute of Technology, Pasadena, USA

ABSTRACT

In anticipation of the upcoming InSight mission, which is expected to deploy a single seismic station on the Martian surface in November 2018, we describe a methodology that enables locating marsquakes and obtaining information on the interior structure of Mars. The method works sequentially and is illustrated using single representative 3-component seismograms from two separate events: a relatively large tele-seismic event (M_w 5.1) and a small-to-moderate-sized regional event (M_w 3.8). Location and origin time of the event is determined probabilistically from observations of Rayleigh waves and body-wave arrivals. From the recording of surface waves, averaged fundamental-mode group velocity dispersion data can be extracted and, in combination with body-wave arrival picks, inverted for crust and mantle structure. In the absence of Martian seismic data, we performed full waveform computations using a spectral element method (AxiSEM) to compute seismograms down to a period of 1 s. The model (radial profiles of density, P- and S-wave-speed, and attenuation) used for this purpose is constructed on the basis of an average Martian mantle composition and model areotherm using thermodynamic principles, mineral physics data, and viscoelastic modeling. Noise was added to the synthetic seismic data using an up-to-date noise model that considers a whole series of possible noise sources generated in instrument and lander, including wind-, thermal-, and pressure-induced effects and electromagnetic noise. The examples studied here, which are based on the assumption of spherical symmetry, show that we are able to determine epicentral distance and origin time to accuracies of \sim 0.5–1° and \pm 3–6 s, respectively. For the events and the particular noise level chosen, information on Rayleigh-wave group velocity dispersion in the period range \sim 14–48 s (M_w 5.1) and \sim 14–34 s (M_w 3.8) could be determined. Stochastic inversion of dispersion data in combination with body-wave travel time information for interior structure, allows us to constrain mantle velocity structure to an uncertainty of \sim 5%. Employing the travel times obtained with the initially inverted models, we are able to locate additional body-wave arrivals including depth phases, surface and Moho (multiple) reflections that may otherwise elude visual identification. This expanded data set is reinverted to refine interior structure models and source parameters (epicentral distance and origin time).

Keywords:
Mars
Waveforms
Marsquakes
Interior structure
Surface waves
Body-waves
Travel times
Surface-wave overtones
Inversion

1. Introduction

Seismology, because of its higher resolving power relative to other geophysical methods for sounding the interior of a planetary

body, has played a prominent role in the study of Earth's interior (e.g., [Dziewonski and Romanowicz, 2007](#)). For example, many of the parameters that are important for understanding the dynamic behavior of planetary interiors are determined by seismology (e.g., [Lognonné and Johnson, 2007](#), [Khan et al., 2013](#)). This is one of the primary reasons for landing a seismometer on Mars with the upcoming InSight (Interior Exploration using Seismic Investiga-

* Corresponding author.

E-mail address: amir.khan@erdw.ethz.ch (A. Khan).

tions, Geodesy and Heat Transport) mission (Banerdt et al., 2013). The InSight mission is currently expected to be launched in May 2018 with deployment on the Martian surface expected the following November. The InSight lander will be the first planetary seismology mission in nearly four decades since the Apollo and Viking missions (e.g., Nakamura, 2015; Anderson et al., 1977; Lognonné and Johnson, 2007) and is expected to provide seismic data from which the internal structure of Mars can be elucidated.

Extra-terrestrial seismology saw its advent with the U.S. Apollo missions which were undertaken from July 1969 to December 1972. Seismic stations were deployed at five locations as part of an integrated set of geophysical experiments. Interpretation and analysis of lunar seismic data proved difficult, because of paucity of stations, limited spatio-temporal configuration, restricted instrument bandwidth, and limited number of usable seismic events (e.g., Lognonné and Johnson, 2007; Khan et al., 2013; Nakamura, 1983, 2015; Kawamura et al., 2015; Knapmeyer and Weber, 2015). In spite of this complexity, it has nonetheless been possible to make first-order inferences on the internal structure that showed the Moon to be a differentiated body, stratified into a crust, mantle, and possibly liquid core (e.g., Nakamura, 1983; Williams et al., 2001; Khan and Mosegaard, 2002; Khan et al., 2004; Lognonné et al., 2003; Gagnepain-Beyneix et al., 2006; Weber et al., 2011; Garcia et al., 2011; Yamada et al., 2014). Continued analysis of this and other data sets keeps refining this picture and, as a consequence, our understanding of lunar structure and its implications for lunar origin and evolution (e.g., Nimmo et al., 2012; Grimm, 2013; Karato, 2013; Yamada et al., 2013; Khan et al., 2014; Pommier et al., 2015; Williams and Boggs, 2015).

InSight will land a single station including a 3-component broadband and short-period seismometer within Elysium Planitia with a nominal lifetime of 1 Martian year (~ 2 Earth years). For seismometer details see Lognonné et al. (2012), Mimoun et al. (2012) and Lognonné and Pike (2015). In addition to the seismic experiment, InSight will carry a probe for measuring heat flow, enable very high-precision measurements of the rotation and precession of Mars, a magnetometer for measuring the magnetic environment around the landing site including crustal and induced fields, and pressure and wind sensors (Banerdt et al., 2013). These data hold the potential of providing significant constraints on the interior structure of Mars much of which remains to be ascertained beyond the first-order picture that currently prevails (e.g., Longhi et al., 1992; Kuskov and Panferov, 1993; Mocquet et al., 1996; Smith and Zuber, 2002; Yoder et al., 2003; Neumann et al., 2004; Wieczorek and Zuber, 2004; Sohl et al., 2005; Verhoeven et al., 2005; Zharkov and Gudkova, 2005; Khan and Connolly, 2008; Rivoldini et al., 2011; Nimmo and Faul, 2013; Wang et al., 2013). From a physical point of view, this includes: 1) crustal structure and thickness; 2) mantle discontinuities; 3) core size, constitution, and state. From knowledge of these parameters, inferences on Mars' bulk chemical composition and thermal state can be drawn, which, in turn, are crucial for constraining its origin and evolution (e.g., Bertka and Fei, 1998; Khan and Connolly, 2008; Taylor, 2013).

Locating marsquakes with a single station is a challenging task as demonstrated by Panning et al. (2015), who tested single-station methods using terrestrial seismic data. Here, we build upon and extend this work by employing the single-station-single-event probabilistic location algorithm developed by Böse et al. (2016) in a purely Martian context. This method estimates source location and uncertainty from observations of surface-wave and body-wave arrivals and their polarization. Surface-wave dispersion data are automatically output as part of the algorithm, which are inverted in combination with body-wave travel time data for radial structure. We illustrate the methodology using two events with different source characteristics to highlight its ability of adapting to different conditions, i.e., data sets, for locating marsquakes.

This study is based on purely radial models and complexities related to anisotropy and three-dimensional structure, particularly in the crust and lithosphere, will undoubtedly complicate the simplified picture envisaged here. However, as the present study seeks to promote a methodology, second-order effects arising from e.g., lateral variations in structure are neglected here and will be the focus of forthcoming analyses. In what follows, the scheme is presented step-by-step, starting with the construction of models of Mars' internal structure, followed by computation of seismograms, including addition of noise, probabilistic marsquake location, and finally inversion for structure. The single-station-single-event probabilistic location algorithm is detailed in our companion paper (Böse et al., 2016).

2. Brief overview of joint location and interior structure determination

The scheme is outlined in Fig. 1 and is divided into four main stages that work as follows.

Input stage (white box): We construct a model of the interior structure of Mars (Section 3) to compute seismic waveforms (Section 4) for two representative events. Waveforms are combined with a realistic noise model (Murdoch et al., 2015a,b) to produce "real" (synthetic) Martian seismic data that form the input for our analysis. The input stage will be replaced with seismic data from Mars as these become available.

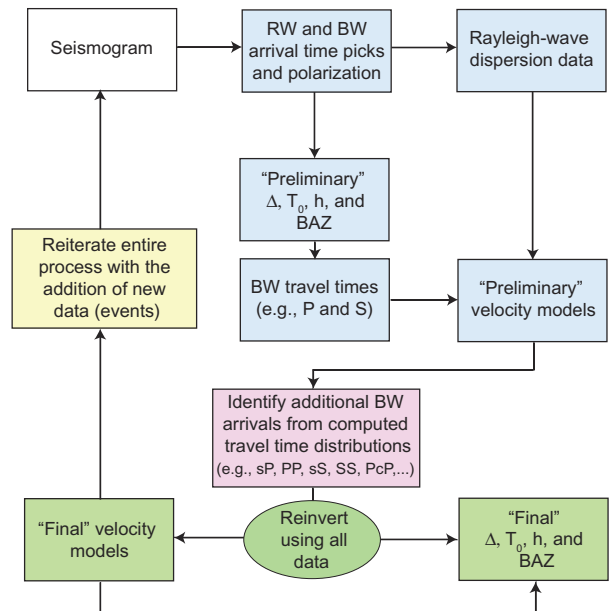


Fig. 1. Joint seismic event-location and structure-inversion scheme. The procedure is divided into four stages. Stage 1 (blue boxes): Rayleigh-wave (RW) and body-wave (BW) arrival time picks and polarization information are obtained from event data (seismogram) and used for "Preliminary" location (here epicentral distance Δ , origin time T_0 , source depth h , and back-azimuth BAZ) determination. For large events both minor- and major-arc Rayleigh wave passages are considered, whereas for small events only the minor-arc surface wave passage is available. Dispersion data are obtained from the surface-wave arrivals and inverted in combination with body-wave arrival picks for a set of "Preliminary" models of interior structure. Stage 2 (red box): Using the "Preliminary" set of inverted models, travel time distributions for other seismic phases (e.g., crustal, depth or core-related phases) can be computed. These distributions can be used as an aid in identifying small-amplitude arrivals that are otherwise difficult to pick visually. Stage 3 (green boxes): Reinversion of refined/updated data set results in "Final" structure models and location estimates. Stage 4 (yellow box): The entire process works iteratively with the addition of new event data. See main text for further details. (For interpretation of the references to colour in this figure caption, the reader is referred to the web version of this article.)

Stage 1 (blue boxes): The method relies on identifying body wave arrivals and the passage of minor- and major-arc surface waves to locate marsquakes in space and time probabilistically given observational uncertainties (Section 5). From observations of surface-waves (Rayleigh) at various frequencies, Rayleigh-wave dispersion is retrieved, which is subsequently inverted jointly with body-wave arrivals for radial models of P- and S-wave speed, density, and source location (Sections 6 and 7.1).

Stage 2 (red box): Inverted models, in turn, are employed to compute expected body-wave travel times for use in refining other arrivals (e.g., PP, PPP, Pcp, ss, SS, SSS, ScS, etc.) that would otherwise elude detection and/or identification (Section 7.2).

Stage 3 (green boxes): Once additional body-wave arrivals have been identified, the expanded data set is reinverted. In this manner, location and model estimates are iteratively improved (Section 7.3).

Stage 4 (yellow box): With the addition of new event data, we repeat the entire procedure and update previous models and event location.

The method is illustrated using a relatively large (M_w 5.1) shallow (5 km depth) event, which is expected to be large enough to result in recordings of multiple surface wave passages along the minor and major arc. However, since current estimates (e.g., Lognonné et al., 1996) suggest that the largest portion of events that will be recorded are small-magnitude ($M_w \leq 4$) local-to-regional events, we also consider a relatively small (M_w 3.8) deep (30 km depth) event, which is only capable of producing surface waves that pass along the minor-arc. Station and event locations are shown in Fig. 2. Since the aim of this study is to demonstrate that the joint source location-interior structure determination is capable of handling both large- and small-magnitude events that result in different data sets, the events considered here are treated separately.

3. Constructing models of Mars' internal structure

The method that we use to construct interior-structure models is based on our previous work Khan and Connolly (2008) and the work of Nimmo and Faul (2013). For brevity, only a cursory description is presented here. We rely on a unified description of the elasticity and phase equilibria of multicomponent, multiphase assemblages from which mineralogical and seismic wave velocity models as functions of pressure (depth) and temperature are constructed. Specifically, we use the free-energy minimization strategy described by Connolly (2009) to predict rock mineralogy,

elastic moduli, and density along self-consistently computed mantle adiabats for a given bulk composition. For this purpose we employ the thermodynamic formulation of Stixrude and Lithgow-Bertelloni (2005a) with parameters as in Stixrude and Lithgow-Bertelloni (2011). Bulk rock elastic moduli are estimated by Voigt-Reuss-Hill (VRH) averaging. The pressure profile is obtained by integrating the load from the surface. Possible mantle compositions are explored within the $\text{Na}_2\text{O}-\text{CaO}-\text{FeO}-\text{MgO}-\text{Al}_2\text{O}_3-\text{SiO}_2$ (NCFMAS) system, which accounts for more than 98% of the mass of the mantle of the experimental Martian model of Bertka and Fei (1997).

Estimates for the Martian mantle composition derive from geochemical studies (e.g., Dreibus and Wänke, 1985; Treiman, 1986; McSween, 1994; Taylor, 2013) of a set of basaltic achondrite meteorites, collectively designated the SNC's (Shergotty, Nakhla, and Chassigny), that are thought to have originated from Mars. Based on the analysis of Dreibus and Wänke, the Martian mantle contains about 17 wt% FeO compared to Earth's upper mantle budget of 8 wt % (e.g., McDonough and Sun, 1995; Lyubetskaya and Korenaga, 2007). This implies a Martian mantle Mg# of 75 (100×molar Mg/Mg + Fe), in comparison to the magnesian-rich terrestrial upper mantle value of ~90. There is little information that bears directly on the thermal state of the Martian mantle as a result of which the areotherm has proved more difficult to constrain (e.g., Verhoeven et al., 2005; Khan and Connolly, 2008). For the computations here, we rely on the "hot" areotherm of Verhoeven et al. (2005) (Fig. 3).

For crustal structure, we rely on a physical parameterization, i.e., P- and S-wave speed, density, and Moho depth as model parameters, rather than thermo-chemical parameters employed in modeling mantle properties. Average crustal thickness is taken from the study of Wieczorek and Zuber (2004) and density, P- and S-wave speed are modeled as increasing linearly from 2 to 3 g/cm³, 4 to 6.5 km/s, and 2 km/s to 3.5 km/s, respectively, between surface and the base of the crust.

As seismic waves propagate in the interior of Mars they are expected to be attenuated with distance much as on Earth. This is a manifestation of an anelastic medium. Another property of a dissipative medium is dispersion, which manifests itself in seismic waves of different frequencies traveling at different speeds. As a consequence, the elastic moduli become complex and frequency-dependent, which provides an appropriate start for the description of viscoelastic dissipation (e.g., Anderson, 1989).

The dissipation model adopted here (for details we refer the reader to Nimmo and Faul (2013)) is based on laboratory experiments of torsional forced oscillation data on melt-free polycrys-

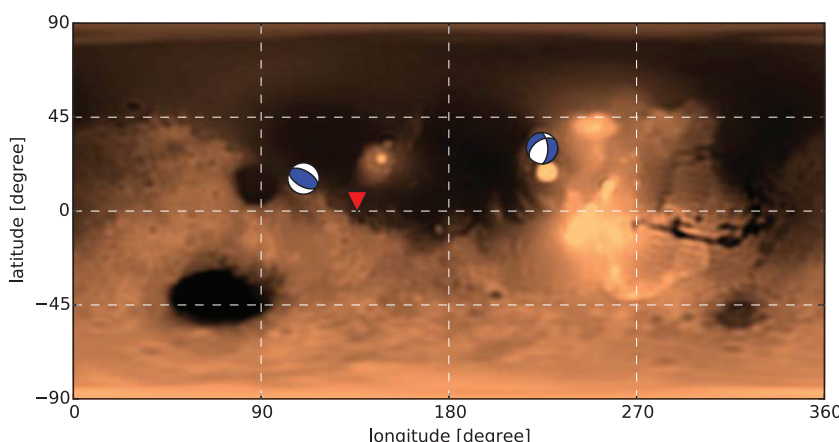


Fig. 2. Location of events (including focal mechanism) and station (red triangle) on the surface of Mars. The M_w 5.1 event is located to the right of the station at an epicentral distance of 86.6° and the M_w 3.8 event to its left at an epicentral distance of 27.6°. Background map shows Martian surface topography. (For interpretation of the references to colour in this figure caption, the reader is referred to the web version of this article.)

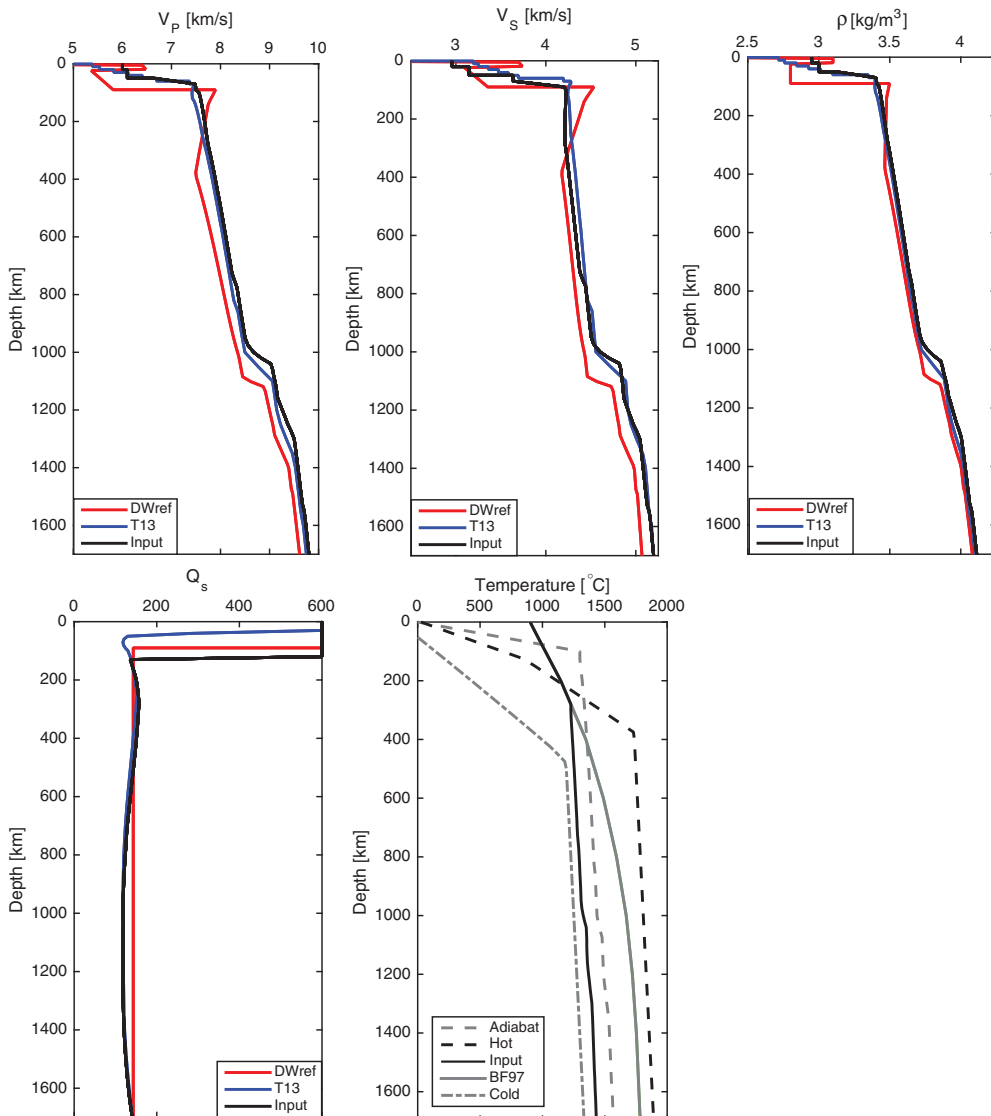


Fig. 3. Computed input (“Input”) radial P-wave speed (V_p), S-wave speed (V_s), density (ρ), and shear attenuation (Q_s) profiles at a period of 1 s based on the bulk Martian composition of [Taylor \(2013\)](#) and the model adiabat (“Input”) shown in the temperature plot. Only crust and mantle structure is shown. For the particular areotherm, mantle, and core composition chosen, the core-mantle-boundary is located below 1800 km depth. Models labeled “DWref” and “T13” are Martian models that have been built using the same methodology described in the main text. The thermal models shown are from [Verhoeven et al. \(2005\)](#) (“Hot” and “Cold”), [Bertka and Fei \(1997\)](#) (“BF97”), whereas “Input” and “Adiabat” represent self-consistently computed mantle adiabats based on the [Taylor \(2013\)](#) composition with a deep and a shallow conductive lithosphere, respectively.

talline olivine and is described in detail in [Jackson and Faul \(2010\)](#). In the absence of melting, dissipation has been observed in the Earth, Moon, and Mars to follow a frequency-dependence of the form $1/Q \sim \omega^{-\alpha}$, where ω is angular frequency and α is a constant (e.g., [Lognonné and Mosser, 1993](#); [Williams et al., 2001](#); [Benjamin et al., 2006](#); [Efroimsky, 2012](#)). α has been determined from seismic and geodetic studies to lie in the range 0.1–0.4 (e.g., [Minster and Anderson, 1981](#); [Benjamin et al., 2006](#)). The failure of Maxwellian viscoelasticity to reproduce this frequency-dependence has led to other rheological models such as the Burgers model (e.g., [Jackson and Faul, 2010](#)). The Burgers model of [Jackson and Faul \(2010\)](#) is preferred over other rheological models because of its ability to describe the transition from (anharmonic) elasticity to grainsize-sensitive viscoelastic behavior as a means of explaining the observed dissipation in the forced torsional oscillation experiments on olivine.

For present purposes, computations were conducted employing a single shear-wave attenuation (Q) model at seismic frequencies (1 s) and a grain-size of 1 cm in accordance with [Nimmo and Faul \(2013\)](#). For the Martian crust and lithosphere, we fixed shear-wave Q to 600 after PREM ([Dziewonski and Anderson, 1981](#)) and to 100 in the core. Dissipation in bulk is neglected and we assume $Q_\kappa = 10^4$ in line with terrestrial applications (e.g., [Durek and Ekström, 1996](#)). Anelastic P- and S-wave speeds ($V_{P/S}$) as a function of pressure (p), temperature (T), composition (c), and frequency (ω) are estimated from the expressions for the visco-elastically computed temperature-, pressure-, and frequency-dependent moduli (further details may be found in [Nimmo and Faul \(2013\)](#)).

The physical properties (isotropic anelastic P- and S-wave speeds, density, and attenuation) so computed are shown in Fig. 3 to a depth of 1700 km. For comparison with sampled seismic

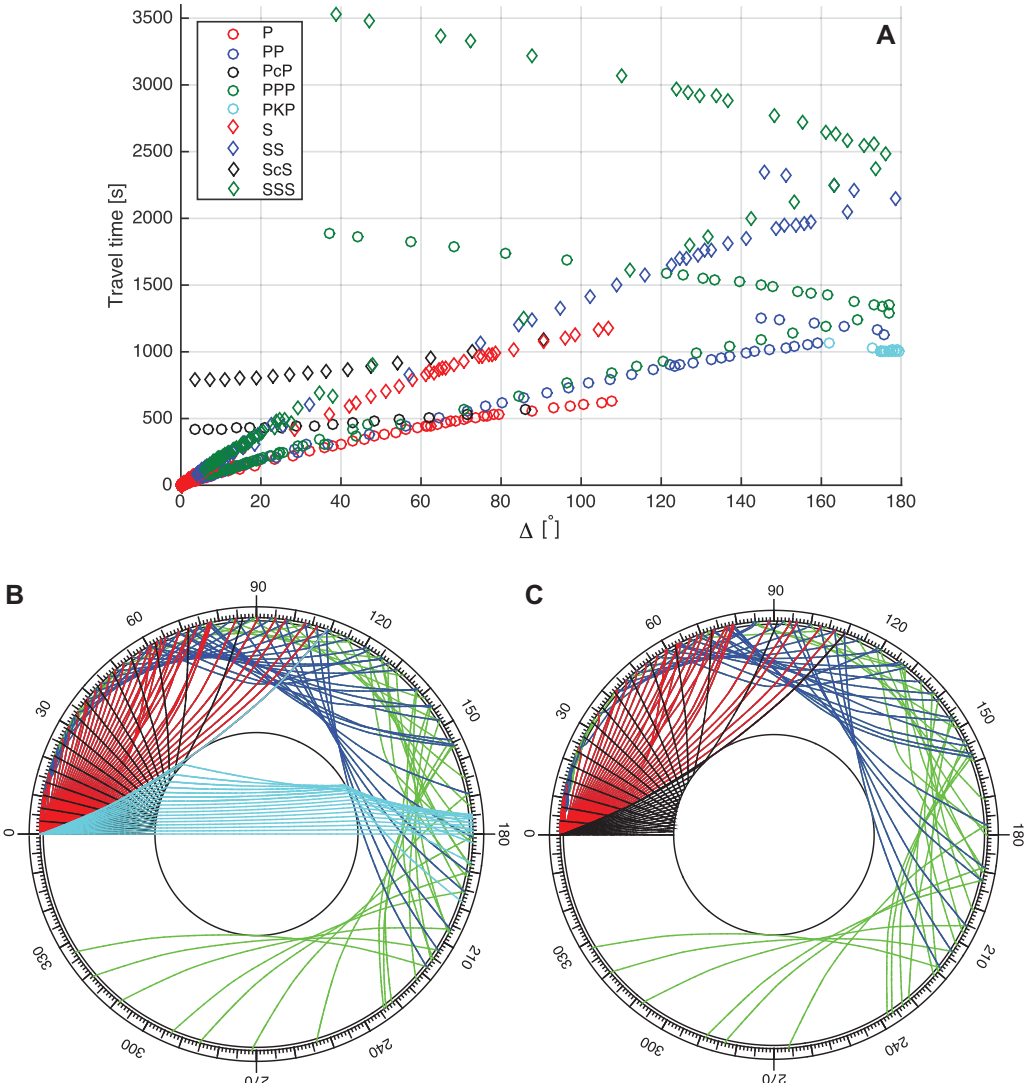


Fig. 4. Travel time curves (A) and ray paths (B–C) for various seismic body-wave phases through the crust and mantle of the Martian “Input” model (Fig. 3) for a 5-km deep source. Raypaths for (B) P, PP, PcP, PPP, PKP, and (C) S, SS, ScS, SSS. Color coding as in (A). For reference, the circle in the center of plots B and C indicates the location of the core-mantle-boundary (1760 km depth), respectively. The plots were created using TtBox (Knapmeyer, 2004). (For interpretation of the references to colour in this figure caption, the reader is referred to the web version of this article.)

wave-speed and density profiles, we are also showing a set of models (DWref and T13) that are constructed in the same manner as the “Input” model, but using a different areotherm to highlight the influence of mantle thermal structure on physical properties. Model DWref is based on the bulk mantle composition of Dreibus and Wänke (1985) and the “Hot” areotherm of Verhoeven et al. (2005) (Fig. 3), whereas model “T13” is computed using the bulk mantle composition of Taylor (2013) and the self-consistently computed adiabat (“Adiabat” in Fig. 3).

These profiles contain prominent features above 400 km and around 1000–1100 km depth. The wave-speed decrease above 400 km depth (DWref only) is due to the steep increase in temperature in the lithosphere that results in a strong low-velocity zone (LVZ) (e.g., Nimmo and Faul, 2013; Zheng et al., 2015). The LVZ zone is not present in the other two models because of a smoother transition between the conductive lithosphere and the mantle adiabat. As shown elsewhere (e.g., Bertka and Fei, 1998; Khan and Connolly, 2008), the discontinuity at ~1100 km depth is linked to the mineral phase transformation olivine→wadsleyite (see also Mocquet et al. (1996) and Verhoeven et al. (2005)), which in Earth is responsible for the “410-km” seismic discontinuity. The associ-

ated shear-wave attenuation structure is also shown in Fig. 3. In the case of “DWref”, the Q-structure is based on PREM, whereas for “Input” and “T13”, we use the viscoelastic approach described above. Generally, shear-wave attenuation structure is observed to be fairly constant throughout most of the mantle in overall agreement with expectations based on PREM and existing Martian models (e.g., Lognonné and Mosser, 1993; Zharkov and Gudkova, 1997; Nimmo and Faul, 2013). Theoretical predictions for the attenuation in the Martian mantle have been discussed by Lognonné and Mosser (1993) and Zharkov and Gudkova (1997). Based on a Q value of 50–150 at the tidal period of Phobos (5 h 32 min) and assuming the absorption band model of Anderson and Given (1982) to hold over the entire frequency range (seismic to tidal), these studies find Q values in the range ~150–400 (at 1 s). For comparison, current estimates of Q at the period of Phobos are 80–105 (e.g., Bills et al., 2005; Lainey et al., 2007; Nimmo and Faul, 2013).

Finally, for the “Input” model described above, we computed raypaths and corresponding travel times for a number of seismic phases (Fig. 4). This figure illustrates the importance of considering travel time information in addition to dispersion data in that the

Table 1

Source and station parameters. Estimated values refer to estimates obtained with P-wave polarization and body-wave (e.g., P, pP, and S) and surface wave travel time information. For source 1 seismic depth phases could not be extracted from the seismograms as a result of which source depth is not inverted for. See main text for details.

Parameter	Value	Estimated values
<i>Station</i>		
Longitude	136°E	
Latitude	4.5°N	
<i>Source 1: M_w5.1</i>		
Longitude	135.3°W	
Latitude	30.1°N	
Depth	5 km	—
Epicentral distance	86.6°	86.5 ± 0.5°
Back azimuth	60°	60.5 ± 0.5°
Origin time (UTC)	18:13:11.15 s	18:13:08.89 ± 3.2 s
<i>Source 2: M_w3.8</i>		
Longitude	110.3°E	
Latitude	15.6°N	
Depth	30 km	29 ± 3 km
Epicentral distance	27.6°	28.2 ± 1°
Back azimuth	295.6°	295 ± 5°
Origin time (UTC)	18:13:11.15 s	18:13:04.89 ± 6.7 s

former are sensitive to much deeper structure than e.g., 40-s Rayleigh-wave group velocities. For example, from Fig. 4 it can be seen that at epicentral distances close to 90°, P- and S-waves bottom in and below the Martian “transition-zone” (~1100 km depth). Moreover, we also observe that the “Input” model does not produce a shadow zone for the direct P- and S-wave arrivals as would be the case for models that contain an LVZ in the upper mantle. As also discussed by Zheng et al. (2015), the seismic signature of an LVZ is the presence of shadow zone for direct P- and S-waves. Range and onset of the shadow zone, however, will depend on location (depth) and strength of a negative velocity gradient. For model “DWref”, for example, the direct P- and S-wave shadow zone covers the epicentral distance ~20°–60°. Finally, much as on Earth, a shadow zone between the direct P- and the PKP-wave is present because of a liquid core in the input model.

4. Computing Martian seismograms

We use the axisymmetric spectral element method AxiSEM (www.axisem.info) (Nissen-Meyer et al., 2014) to compute a database of Green’s functions for the 1D Martian model described above. These include the full numerical solution of the visco-elastic wave equation including effects related to attenuation and are accurate down to 1 s period for body waves and 3 s for surface waves. We neglect effects of ellipticity, rotation, and gravity. Rotation and gravity have a small effect in the frequency range of interest here (~1–100 s). Ellipticity is expected to be stronger than on Earth and will be treated in future applications (see also Böse et al., 2016). Effects arising from crustal heterogeneities (e.g., surface and Moho topography, lateral variations in properties) have been discussed by Larmat et al. (2008).

In a second step, we use Instaseis (van Driel et al., 2015) to extract seismograms from the aforementioned Green’s function databases. These employ higher-order spatial and temporal interpolation to maintain the accuracy of the spectral element method. The method has been benchmarked down to periods of 2 s for Earth against the full waveform method Yspec of Al-Attar and Woodhouse (2008). The Instaseis code is available at www.instaseis.net and allows for both moment tensor (marsquake) and single force (impact) sources. As this approach is based on a precomputed database, it allows us to quickly compute seismograms and verify our method for a variety of sources.

Because no marsquakes were unambiguously detected during the Viking missions (e.g., Anderson et al., 1977), there is no direct observation of the seismicity of Mars. As documented elsewhere (e.g., Phillips, 1991; Golombek et al., 1992; Knapmeyer et al., 2006; Lognonné and Johnson, 2007; Teanby and Wookey, 2011), current estimates allow for a relatively large range in Martian seismicity, but appear to be compatible with the occurrence of ~1–10 events with seismic moment around 10^{17} N m during the nominal lifetime of the experiment (2 Earth years). 3rd-orbit passages of Rayleigh waves are expected to become observable within the moment range 10^{16} – 10^{18} N m (e.g., Lognonné et al., 1996; Panning et al., 2015), which is important for the use of surface-wave-based marsquake location (see Section 5). For the more numerous intermediate- and small-sized events where multiple surface-wave passages will be unavailable, location will rely on the use of minor-arc surface-wave passages and body-wave travel time information. This will be discussed in more detail in the following section.

The sources used here for illustration include a large M_w 5.1 ($\sim 1 \cdot 10^{17}$ N m) and a small M_w 3.8 ($\sim 5 \cdot 10^{14}$ N m) event that are located at epicentral distances of 86.6° and 27.6°, respectively. Similar events are contained in the “medium” catalogue by Knapmeyer et al. (2006), which is based on extensive mapping of compressional and extensional faults observed in the MOLA (Mars Orbiting Laser Altimeter) shaded relief maps. This can be related to seismicity by invoking various assumptions about the annual seismic moment budget, the moment-frequency relationship, and a relation between rupture length and released moment. While location, moment, depth, strike, and dip are defined in the catalogue, rake angle was added as a uniformly distributed random number. Source and station parameters are catalogued in Table 1.

Realistic noise is added to the computed traces based on the current model of the InSight noise model working group Murdoch et al. (2015a,b) and previous work of Lognonné and Mosser (1993) and Van Hoolst et al. (2003). The noise model considers contributions from all possible ambient noise sources: wind effects on the instruments and the lander, pressure compacting the regolith, direct thermal effects on the instrument, thermo-elastic effects on the tether and the levelling system, electric and magnetic field effects on the instruments and the tether, and instrument-related noise (self-noise of the electronics and digitizer noise). The model predicts the power spectral density (psd) of the expected noise, which is compared to the high- and low-noise

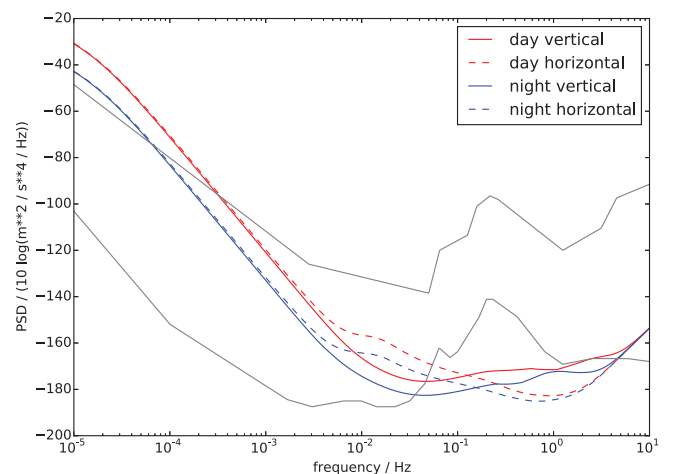


Fig. 5. Expected noise levels for the seismic instrument to be deployed on Mars. Shown are noise levels for both horizontal and vertical components as well as for night and day time. For comparison, the new low-/high-noise model for the Earth by Peterson (1993) is also shown. See main text for details.

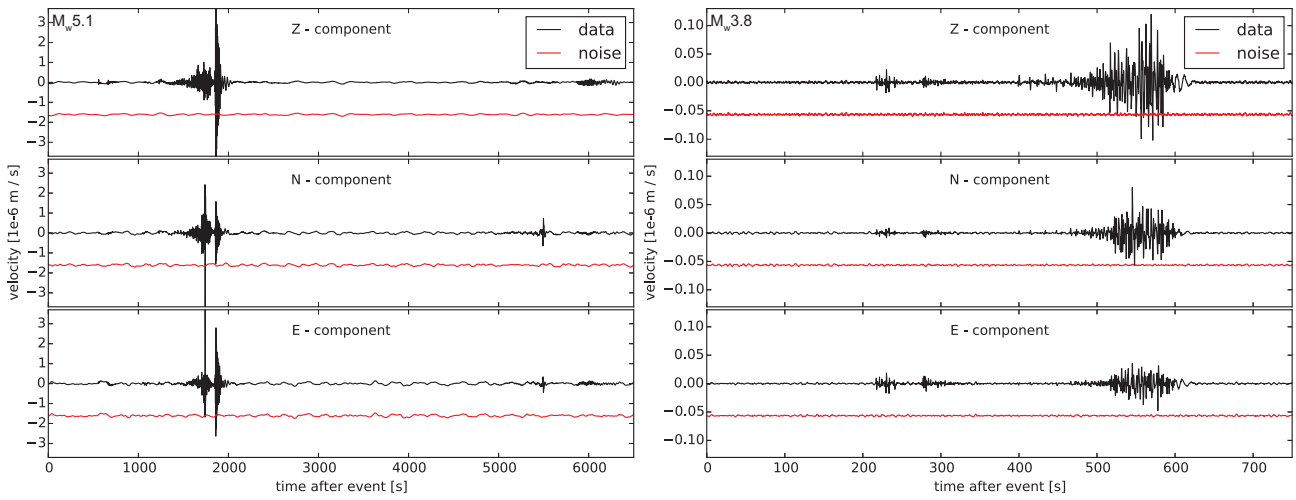


Fig. 6. Three-component (vertical – Z; horizontal – N and E) synthetic waveforms computed (up to 1 s period) with AxiSEM for two events: a 5-km deep marsquake (M_w 5.1) located at an epicentral distance of 86.6° and a 30-km deep marsquake (M_w 3.8) located at an epicentral distance of 27.6° . Both events are taken from the catalogue compiled by Knapmeyer et al. (2006). The seismic model employed in computing the seismograms is shown in Fig. 3. Source location is summarized in Table 1. Time series of seismic noise based on the noise model (Fig. 5) are shown underneath each component in red. Note the relatively low-frequency content of the noise, which becomes dominant for periods greater than 100 s. In line with the noise model (Fig. 5), the horizontal noise components contain more high-frequency noise relative to the vertical noise component. For the M_w 5.1 event, arrivals appearing around 5500 s relate to surface-wave overtones. Seismograms are filtered in the passband 2–200 s (M_w 5.1) and 0.5–10 s (M_w 3.8), respectively. (For interpretation of the references to colour in this figure caption, the reader is referred to the web version of this article.)

model of the Earth (Peterson, 1993) in Fig. 5 for both night and day as well as vertical and horizontal components. The main difference is the absence of the microseismic peaks that results in much lower noise levels in the body-wave frequency range and a stronger increase towards lower frequencies due to thermally-generated noise on Mars. To be conservative in our analysis, we use the “day-side” noise model. Finally, to create time-domain noise from the predicted psd, random phases with uniform distribution were assumed, because of lack of phase information in the noise model.

The resulting three-component synthetic velocity seismograms filtered in the passband 1–200 s period are shown in Fig. 6. While the large amplitudes are caused by minor-arc short-period surface waves, both body waves and major-arc surface waves are clearly visible above the noise level for these particular events. The relatively large-amplitude short-period surface waves are unrealistic and caused by adherence to spherical symmetry. However, as we only invert surface waves with periods from ~ 14 s and up (see Section 7.1 for further details), the short-period surface waves are unlikely to interfere. Moreover, such short-period surface waves are unlikely to be observed due to scattering in the heterogeneous crust (Gudkova et al., 2011). A quantitative analysis of this effect will be the subject of future work.

5. Probabilistic marsquake location

Locating marsquakes with a single station is a challenging task. Here, we apply the probabilistic framework for single-station location by Böse et al. (2016) that combines multiple algorithms to estimate source location and uncertainties from phase arrivals and the polarization of surface and body waves. Because noise is expected to be lower on the vertical component (by terrestrial experience and predictions of the current Martian noise model) in comparison to the horizontal components, we focus on the use of Rayleigh waves rather than Love waves.

Briefly (for details the reader is referred to Böse et al., 2016), for large marsquakes epicentral distances and origin times are estimated from multi-orbit Rayleigh-phase arrivals R1, R2, and R3 (R1 propagates from the source towards the receiver along the minor-arc; R2 circles the planet in the opposite direction along the major arc; R3 travels along the minor arc and makes another trip around the great-circle path) as described in Panning et al.

(2015), in addition to picks of body-wave phases (e.g., P- and S-waves). For the anticipated more numerous smaller events, we rely on the observation of body-wave phases and minor-arc (R1) surface-wave arrivals. Back azimuth between receiver and marsquake is determined for all events from the polarization of the R1 and P-wave phases. (e.g., Selby, 2001; Chael, 1997; Eisermann et al., 2015). Estimates from the various methods are combined through the product of their probability density functions, resulting in an improved event location estimate compared to the results that would be obtained if each algorithm were to be applied independently.

To run the procedure, we low-pass filter the vertical component of the simulated seismogram for the large M_w 5.1 event (Fig. 6) in a series of 35 (half octave-wide) band-pass filters from 15 s to 100 s using a zero-phase 2nd-order Butterworth filter with 20% overlap. For each band, we computed waveform envelopes and picked peak amplitudes of R1, R2, and R3 as the time of arrival of the peak energy (Fig. 7). The epicentral distance and origin time are computed from the arithmetic means taken over all bands, whereas uncertainties are estimated from the standard deviation assuming normal distributions. Group velocities in the various frequency bands (dispersion data) are extracted for purposes of obtaining information on internal structure as described in more detail in Section 6.

For the small M_w 3.8 event, R2 and R3 surface-wave arrivals cannot be identified. Instead, we determine epicentral distance and origin time by picking P-, S-, and R1-arrivals in the seismogram and by comparing the resulting differential times with those computed theoretically using a newly constructed database of Martian models. This model database (hereinafter “Event location model database”) consists of several thousand models that were obtained in a similar manner to Khan and Connolly (2008), i.e., by inversion of areodetic data (mean mass and moment of inertia), but using the updated parameterization and thermodynamic data described in Section 3. The models are shown in Supplementary Material (Fig. S1). It should be emphasized that the “Event location model database” is only used for the purpose of locating events and is not employed for retrieving information on interior structure. For details on event location, the reader is referred to Böse et al. (2016).

For the two events, we determine most probable locations corresponding to epicentral distances of $86.5^\circ \pm 0.5^\circ$ and $28.2^\circ \pm 1^\circ$,

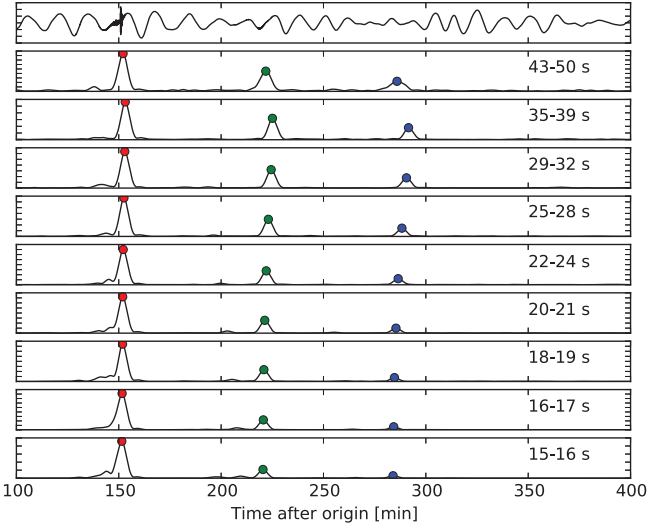


Fig. 7. Frequency-dependent waveform envelopes for the $M_w 5.1$ event. The vertical component of the synthetic waveforms (shown in the top panel and shown filtered in the frequency range 0.01–0.5 Hz) is low-pass filtered in a series of band-passes (indicated on the right of each panel). Waveform envelopes are shown for each band-pass, from which arrival times of orbiting Rayleigh waves (R1 – red, R2 – green, and R3 – blue) are obtained. (For interpretation of the references to colour in this figure caption, the reader is referred to the web version of this article.)

back azimuths of $60.5 \pm 0.5^\circ$ and $295 \pm 5^\circ$, and origin times of $18:13:08.9 \pm 3.2$ s and $18:13:04.9 \pm 6.7$ s, respectively. In comparison, the origin time estimate errors determined by Panning et al. (2015) are larger, reflecting improved origin-time determination through addition of body-wave arrival times in this study. Absolute event locations are found by combining the epicentral distance and back-azimuth estimates. To determine source depth, we rely on the observation of depth phases (e.g., pP, sP, and sS). The paths of these phases closely follows that of the direct P-wave and result from a surface reflection in the vicinity of the event. The separation of P and pP/sP (similarly for S and sS) increases with increasing source depth and the time delay between e.g., P and pP/sP is approximately proportional to the depth of the event. For the $M_w 3.8$ event, pP could be identified, which resulted in an initial depth estimate of 29 ± 3 km. For the $M_w 5.1$, where no depth phases could be resolved, we assume the event to be shallow and use a prior on source depth based on the catalogued depth distribution compiled by Knapmeyer et al. (2006). The retrieved locations are in good agreement with actual source parameters (see Table 1). It should be emphasized that these estimates are based on spherically symmetric models and do not consider effects arising from ellipticity, topography, and structural variation in the crust.

To test for reliability of the location in the case of a deep event, we recomputed seismograms for the large $M_w 5.1$, but at 50-km depth. As for the shallow event, we observed and were able to pick all surface-wave passages of R1, R2, and R3. The derived dispersion characteristics were similar to the shallow event, but comprised a narrower frequency range (~ 15 – 30 s), based on the increase in noise with period (see Fig. 5).

6. Inversion of Rayleigh-wave dispersion data and body-wave travel times

6.1. Modeling aspects

In this section we describe the inversion of the surface-wave dispersion and body-wave travel time data obtained in the previous section for radial profiles of crust and mantle structure. The

inversion methodology follows previous approaches (e.g., Khan and Mosegaard, 2002) and only the main computational aspects are considered here.

We employ the probabilistic approach of Mosegaard and Tarantola (1995) to solve the non-linear inverse problem posited here. Within the Bayesian framework, the solution to the inverse problem $\mathbf{d} = g(\mathbf{m})$, where \mathbf{d} is a data vector containing observations and g a typically non-linear operator that maps a model parameter vector \mathbf{m} into data, is given by

$$\sigma(\mathbf{m}) = kf(\mathbf{m})\mathcal{L}(\mathbf{m}), \quad (1)$$

where k is a normalization constant, $f(\mathbf{m})$ is the prior probability distribution on model parameters, i.e. information about model parameters obtained independently of the data under consideration, $\mathcal{L}(\mathbf{m})$ is the likelihood function, which can be interpreted as a measure of misfit between the observations and the predictions from model \mathbf{m} , and $\sigma(\mathbf{m})$ is the posterior model parameter distribution containing the solution to the inverse problem. The particular form of $\mathcal{L}(\mathbf{m})$ is determined by the observations, their uncertainties and how these are employed to model data noise.

For present purposes, we assume Rayleigh- and body-wave data noise to be uncorrelated and described by a Laplacian distribution (L_1 -norm), which results in a likelihood function of the form

$$\mathcal{L}(\mathbf{m}) \propto \exp \left(-\sum_{\omega} \frac{|\mathbf{d}_{\text{obs}}^{\text{R}} - \mathbf{d}_{\text{cal}}^{\text{R}}|}{\sigma_{\text{R}}} - \sum_i \frac{|\mathbf{d}_{\text{obs}}^{\text{T}} - \mathbf{d}_{\text{cal}}^{\text{T}}|}{\sigma_{\text{T}}} \right) \quad (2)$$

where \mathbf{d}_{obs} and \mathbf{d}_{cal} denote vectors of observed and calculated data of frequency-dependent fundamental-mode Rayleigh-wave group velocities (R) and body-wave travel times (T) respectively, ω frequency, and σ data uncertainty. Determining σ_{R} is less straight forward and presently σ_{R} is set to $\pm 3\%$ of the group velocity based on visual inspection of the width of the Rayleigh-wave envelopes. σ_{T} for each body-wave travel time pick T_i is assessed directly from the seismic data.

To sample the posterior distribution (Eq. (1)) we employ the Metropolis algorithm. Although this algorithm is based on random sampling of the model space, only models that result in a good data fit and are consistent with prior information are frequently sam-

Table 2

Model and data parameters, prior range (prior information), and connections between the various parameters (physical laws). Note that we only invert for primary parameters; secondary parameters are conditional, i.e., depend on primary parameters. Primary parameters are all log-uniformly distributed.

Model parameters	Prior range	Description
X	Fixed	Composition (primary)
T_m	500–2000 °C	Adiabatic temperature at d_{ad} (primary)
d_{Moho}	20–100 km	Moho thickness (primary)
d_{ad}	100–600 km	Depth to conductive areotherm-adiabat crossing (primary)
R_{core}	1300–3000 km	Core radius (primary)
h	0–100 km	Source depth (primary)
M		Equilibrium mineralogy (secondary)
V_p, V_s		Isotropic (anelastically-corrected) P- and S-wave speed (secondary)
ρ		Density (secondary)
Q		Attenuation (secondary)
<i>Data parameters</i>		
C_R		Rayleigh-wave group velocity (data)
T_i		Body-wave travel times (data)
<i>Method</i>		
g_1		Thermodynamic modeling
g_2		Equation-of-state modeling
g_3		Anelastic correction
g_4		Prediction of surface-wave dispersion and body wave travel times

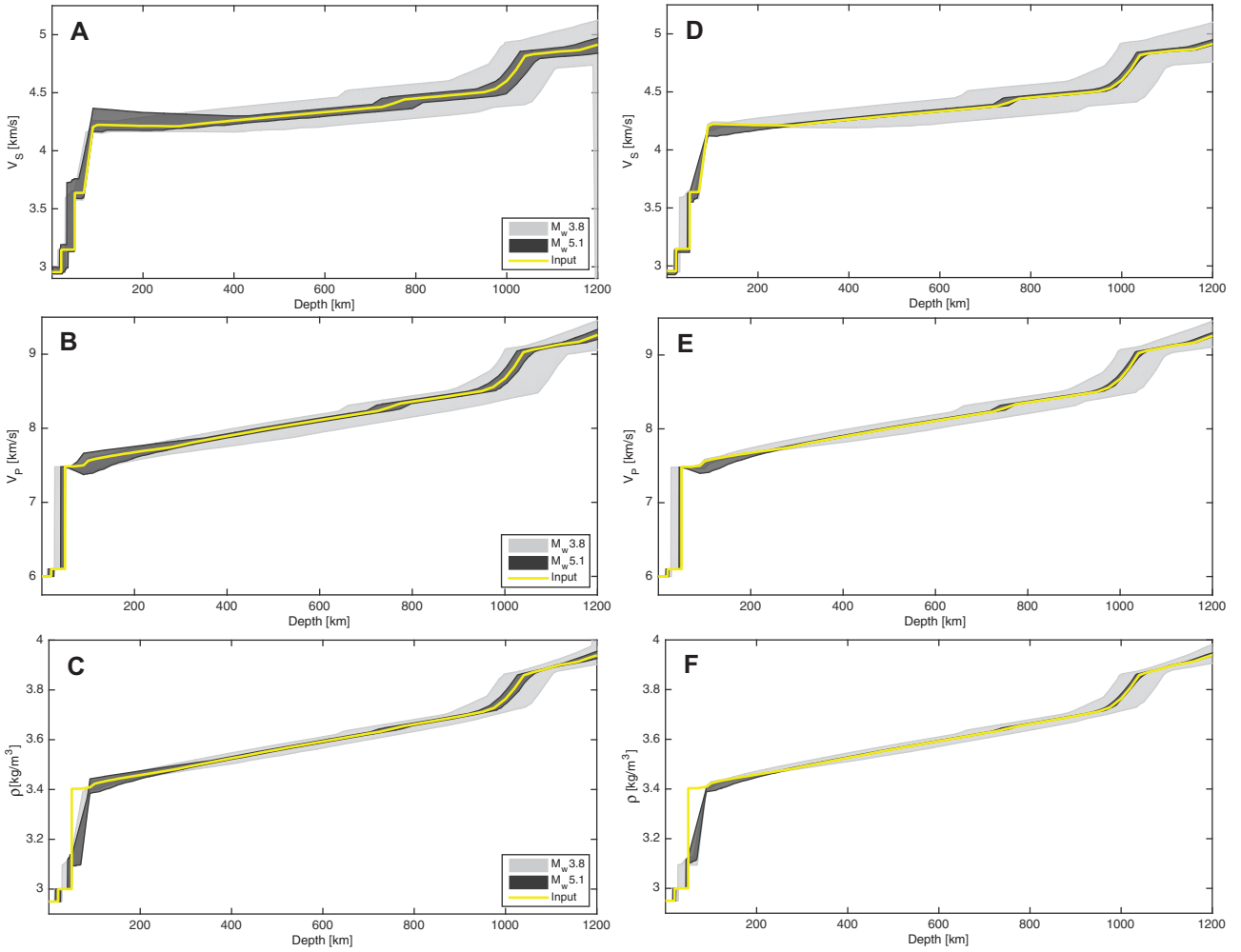


Fig. 8. “Preliminary” (A–C) and “Final” (D–F) inverted Martian models. Shown are profiles of S-wave speed (A, D), P-wave speed (B, E), and density (C, F). Envelopes encompass all sampled models. “Input” designates the input model (Fig. 3) employed for computing Martian seismograms. “Preliminary” inverted models are based on dispersion and P- and S-wave travel time data. “Final” inverted models are based on dispersion and the expanded travel time data set (see Table 3). The M_w 5.1 event is located at an epicentral distance of 86.6° as a result of which rays sample deeper than in the case of the regional M_w 3.8 event (27.6°).

pled (importance sampling). The Metropolis algorithm is capable of sampling the model space with a sampling density proportional to the target posterior probability density without excessively sampling low-probability areas [Mosegaard and Tarantola \(1995\)](#).

The entire forward model consists in computing Rayleigh-wave group velocity dispersion data (fundamental-mode Rayleigh-wave group velocities are calculated using the minor-based code of [Nolet \(2008\)](#)) and body-wave travel times from radial P- and S-wave and density profiles. To compute stable mineralogy, seismic wave speeds, and density along a self-consistent mantle adiabat for a given composition, we rely on free-energy minimization as described in [Connolly \(2009\)](#). Based on this, the forward problem can be summarized as

$$\{X, T_m, d_{\text{Moho}}, d_{\text{ad}}, R_{\text{core}}, h\} \xrightarrow{g_1} M \xrightarrow{g_2, g_3} \{\rho, V_S, V_P\} \xrightarrow{g_4} \{C_R(\omega), T_i\}$$

where the following parameters are the primary parameters that are varied in the inversion: bulk mantle composition (X), temperature (T_m) at the location (depth) (d_{ad}) where the conductive lithosphere intersects the mantle adiabat, Moho depth d_{Moho} , core radius (R_{core}), and source depth (h). Equilibrium mineralogy (M), physical properties (ρ, V_S, V_P) define secondary, conditional, parameters and depend on the primary parameters. $C_R(\omega)$ and T_i are frequency-dependent surface-wave dispersion data and body-

wave travel times, respectively. All model parameters, including forward modeling routines (g_1, g_2, \dots) are summarized in Table 2.

The intervals within which the primary parameters are sampled are log-uniformly distributed within wide bounds. This prior information ($f(\mathbf{m})$ in Eq. (1)) represents a “minimal prior” that samples wide ranges for the individual parameters with bounds set by various laboratory measurements. These upper and lower limits are delineated in Table 2 and are much larger than InSight mission requirements ($\pm 5\%$ for S-wave speed).

7. Results and discussion

In discussing results, we follow the scheme outlined in Fig. 1 and consider the four-stage analysis procedure described previously. The fourth stage, which involves reiterating the entire procedure sequentially with new data, will be applied in the future.

7.1. Stage 1: Preliminary inversion

Fig. 8 shows retrieved seismic P- and S-wave speed and density profiles and their fit to data (Fig. 9) for both events. Dispersion data computed using the “Input” model show the same trend across the observed frequency range as those extracted from the seismic data and, within uncertainties, similar group velocities. Inverted seismic

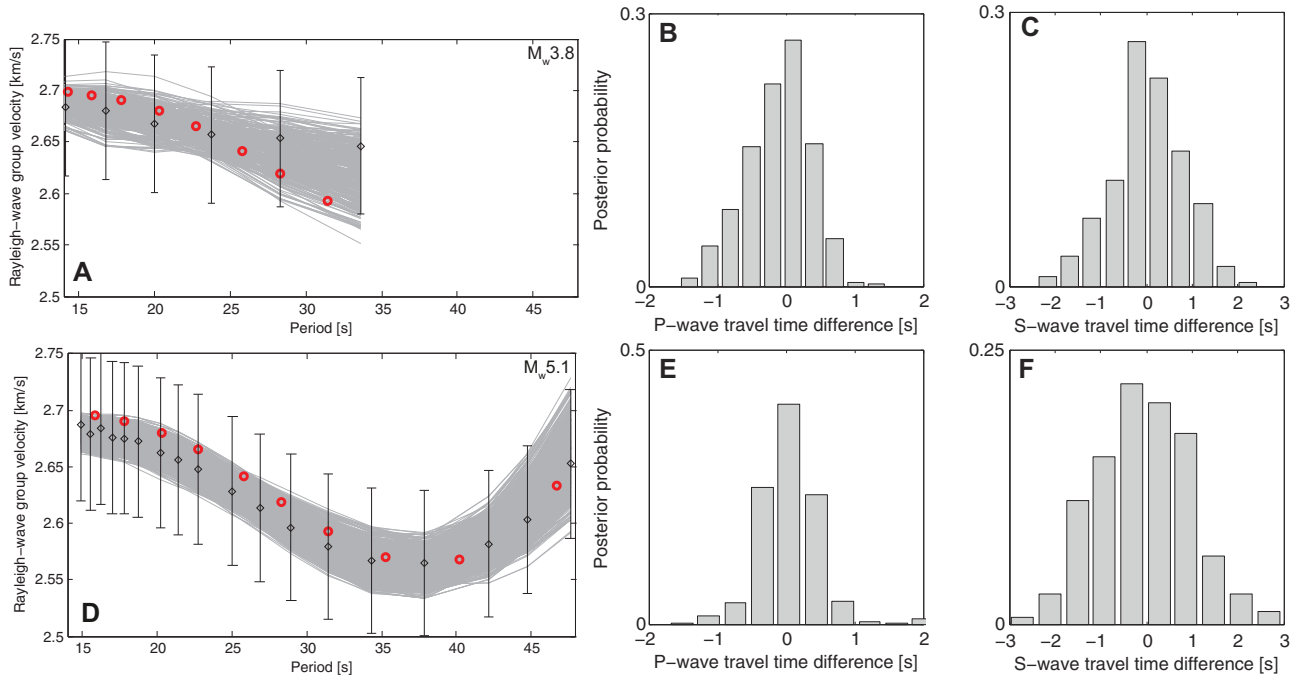


Fig. 9. Comparison of observed and calculated data based on the inverted models shown in Fig. 8. (A, D) Calculated (gray lines) and observed Rayleigh-wave group velocities (circles) including uncertainties (error bars) and group velocities computed for the “Input” model shown in Fig. 3 (red circles). Travel time differences between computed and observed P- (B, E) and S-wave arrivals (C, F). (For interpretation of the references to colour in this figure caption, the reader is referred to the web version of this article.)

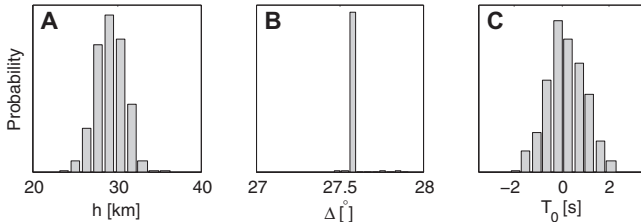


Fig. 10. Re-located source parameters for the $M_w3.8$ event: (A) source depth (h); (B) epicentral distance (Δ); and (C) origin time (T_0). For comparison, input source parameters are given in Table 1.

models are found to agree well with the “Input” model (compare with yellow profile). Major features such as depth to Moho, absolute velocities, and densities are all captured in the inverted models. Note that all models shown have large likelihood values, i.e., fit observations within observational uncertainties (specified in Section 6). Differences between the inverted profiles for the two events are apparent in the relative widths of sampled models, which reflects the increased epicentral distance resulting in P- and S-waves that sample a much larger portion of the mantle than is the case for the smaller regional event, in addition to dispersion data that span a larger frequency range. From analysis of the profiles, we find that the Rayleigh-wave dispersion data are mainly sensitive to S-wave speeds and that sensitivity extends to $\sim 200\text{--}250$ km depth. To illustrate the simultaneous inversion for source location, inverted source parameters (epicentral distance, origin time, and source depth) for the $M_w3.8$ event are shown in Fig. 10. These are found to be in good agreement with the input parameters (c.f., Table 1). Interior structure and source location will be updated in the following through the addition of more data.

7.2. Stage 2: Iterative refinement – Identifying body-wave arrivals

Simultaneously with model inversion performed in stage 1, travel times for a series of body-wave phases are computed for all

inverted models shown in Fig. 8. For this purpose we use the TauP toolkit (Crotwell et al., 1999). The resultant travel time distributions are employed as a means of identifying additional arrivals that would otherwise be difficult to assign and/or pick visually. This procedure is illustrated in Fig. 11, which shows the computed travel time distributions for the various phases overlain directly on the seismograms. Proceeding thus, we are able to identify a number of additional phases such as sP and sS that help constrain source depth, in addition to reflections from the surface (SS and SSS; see Fig. 4) and Moho (P^mP and SmS). Standard body-wave nomenclature and ray paths can be found at <http://www.isc.ac.uk/standards/phases/>. What we observe is that depending on which event is analyzed, some phases are easier to discriminate than others, particularly those that relate to depth (pP, sP, and sS). As expected, depth phases are easier to identify in the case of the deep $M_w3.8$ event because these are well separated from the P- and S-wave arrivals unlike for the shallow $M_w5.1$ event. We have tried to pick phases as consistently as possible using the computed travel time distributions as primary guidance, but have nonetheless adjusted various picks according to personal judgement. This might possibly introduce inconsistencies, which could be offset by increasing the uncertainty on arrival time picks. The additional seismic phases thus identified for the two events are tabulated in Table 3.

We also computed travel-time distributions for typically very small-amplitude phases that are notoriously difficult to pick even with high-quality terrestrial seismic data. Picking core phases PcP and ScS , which are of importance for estimating core radius, reliably from a single seismogram is difficult. These phases typically only become visible after stacking of many seismograms. This is, however, unlikely to become a standard procedure in the context of InSight on Mars. Computed PcP and ScS travel time distributions encompass the theoretically predicted PcP and ScS arrivals, but are too wide to allow us to unambiguously discriminate the correct arrival (Fig. 12). The large variations in computed PcP and ScS travel times reflect the circumstance that inversion of

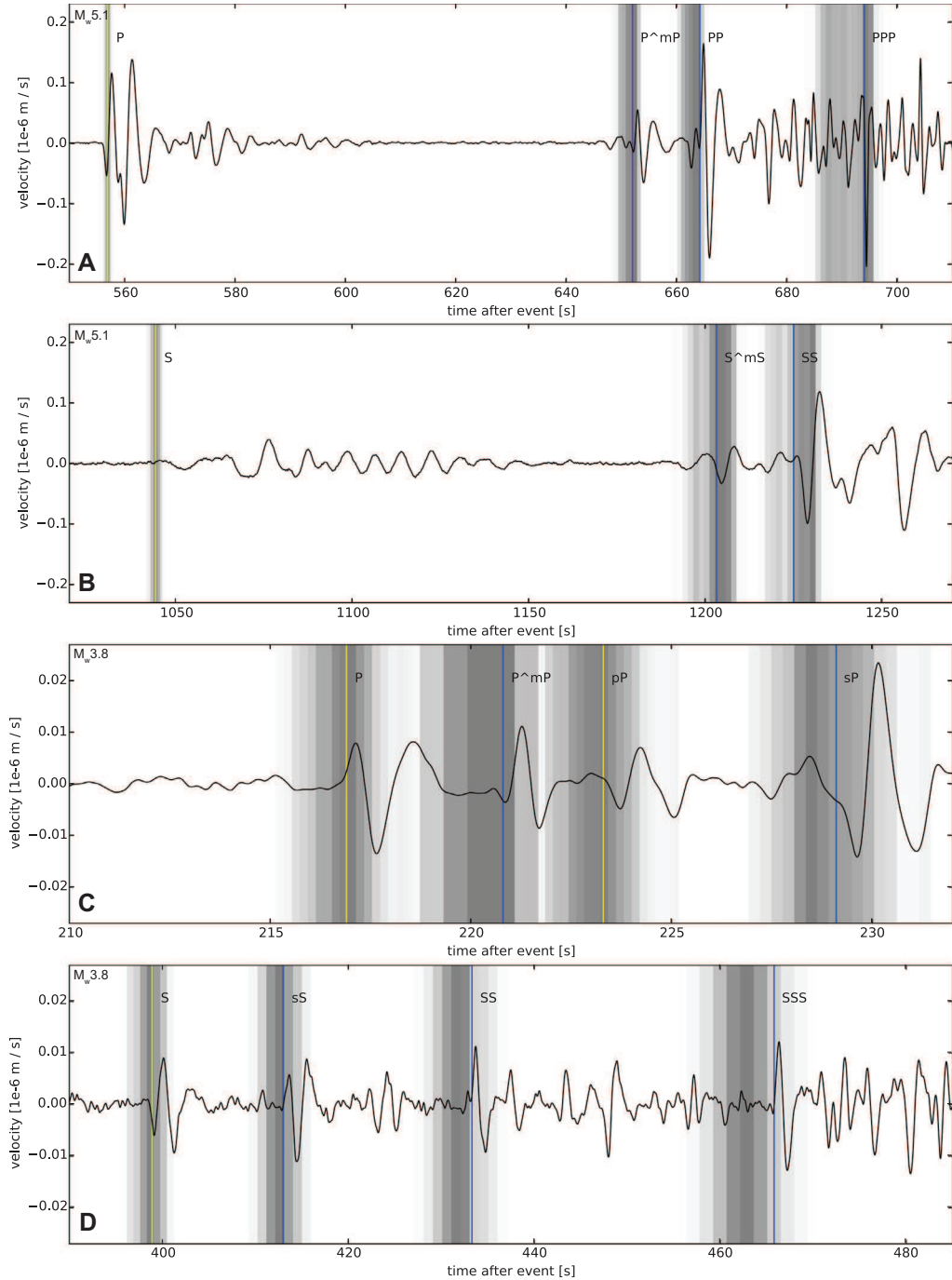


Fig. 11. Comparison of computed (vertical gray bars) and manually identified (vertical colored lines) body-wave arrivals for different seismic body-wave phases: plots A and B illustrate P- and S-wave phases for the $M_w 5.1$ event and plots C and D show P- and S-wave phases for the $M_w 3.8$ event. The distributions of computed travel times estimated from the preliminary inverted models (Fig. 8) are shown as histograms (vertical gray bars) where probability of occurrence scales with color: white (least probable)–black (most probable). Vertical yellow lines refer to travel times obtained from manual inspection of the seismograms used for the preliminary inversion and blue lines denote our picks once computed travel time distributions are available (see Table 3). Waveforms have been filtered (using a causal Butterworth filter) in the period range 1–5 s (plots A, C, and D) and 1–20 s (plot B). Only vertical-component data are shown. Note that some phases such as the S-wave arrival for the $M_w 5.1$ event have been picked on the horizontal components (see Fig. 12). (For interpretation of the references to colour in this figure caption, the reader is referred to the web version of this article.)

surface-wave dispersion data and P- and S-wave arrivals are, as expected, ill-suited to constrain core radius. Note that although Pcp/Scs arrivals appear in some cases to overlap the direct P/S arrivals, i.e., arrive prior to the latter, this is actually not the case because the corresponding P- and S-wave arrivals arrive earlier than indicated by the yellow line in the figure. On a more speculative note, we envision that a core phase may possibly be picked with reasonable certainty so as to provide a useful first-order esti-

mate of core radius once several events have been analyzed sequentially, i.e., once a travel time database has been built up.

Finally, we should note that the identification of seismic arrivals performed here is not exhaustive; for the purpose of illustrating the methodology we concentrated on the most obvious signals and complex signal related to crustal reverberations (apparent for the $M_w 5.1$ event immediately after the first P- and S-wave arrivals between ~ 570 – 600 s and ~ 1070 – 1150 s, respectively), for

Table 3

Predicted and manually picked body-wave travel times, including pick uncertainty, for the seismic phases that could be identified initially (marked with *) and after preliminary inversion. Predicted travel time refers to travel times computed from the “Input” model shown in Fig. 3. Manually picked travel times are obtained from visual inspection of the synthetic seismograms. No picks were made for the core phases PcP and ScS because inversion based on dispersion data and P- and S-wave arrivals is not able to constrain lower mantle structure/core size (see Fig. 12).

Phase	Predicted travel time (s)	Picked travel time (s)
<i>Source 1 ($M_w5.1$)</i>		
P^*	556.9	556 ± 1
PcP	569.0	—
P^*mP	650.5	652.0 ± 2
PP	662.4	664.2 ± 2
PPP	689.3	694.0 ± 2
S^*	1044.4	1044.4 ± 1
ScS	1068.1	—
S^*mS	1200.8	1203.2 ± 2
SS	1225.4	1225.0 ± 2
<i>Source 2 ($M_w3.8$)</i>		
P^*	217.4	216.9 ± 1
P^*mP	221.3	221.0 ± 1
pP^*	223.3	223.9 ± 2
sP	229.1	229.5 ± 2
S^*	399.6	398.9 ± 1
sS	414.0	413.0 ± 2
SS	433.3	432.3 ± 2
SSS	465.8	465.4 ± 2

example, is not considered. On a more general note, assigning phases can be challenging and while the use of travel time predictions based on “Preliminary” inverted models presents a promising means for picking additional phases, assigning body-wave arrivals will nonetheless depend crucially on the background noise level. Thus, although mislabeling of seismic phases is potentially possible, we expect that in a subsequent inversion the wrongly assigned phase can not be fit, as a result of which the potential outlier can be isolated and relabeled. This procedure summarizes iterative refinement, a central theme of the methodology proposed herein.

7.3. Stage 3: “Final” inversion

With the additional arrivals, the entire data set is reinverted for a new set of interior structure models and source parameters (epicentral distance and origin time). The “Final” models are shown in Fig. 8. Comparison with “Preliminary” models shows, as expected, the additional gain in information obtained through inversion of

the expanded travel time data set. Proceeding in this manner, we can iteratively improve our results as data become available by continuously building upon and refining previous models and event locations (stage 4).

In summary, data-constrained pre-selection and refinement of the location of seismic phases presents a powerful complimentary means of obtaining additional information. In particular, as data and events accumulate, continuous refinement and narrowing of the travel time and model parameter distributions will likely be the means by which progress will be achieved. However, the feasibility of the present approach will depend strongly on the nature of the data and sources that will be recorded, including installation characteristics, level of background seismic noise on Mars, and Martian seismicity.

8. Conclusion and summary remarks

In this study, we have described a methodology that, based on a representative set of 3-component seismograms from single events, (1) determines location, origin time, and back azimuth of marsquakes probabilistically using surface- and body-wave travel time information, in addition to P-wave and surface-wave polarization; (2) extracts information on surface-wave dispersion characteristics and inverts this information in combination with body-wave travel times for 1D models of interior structure; (3) employs the inverted models to produce travel time distributions of additional body wave phases as an aid in picking arrivals where identification is otherwise difficult or unfavorable; (4) reinverts the expanded data set for a new set of interior structure models and source parameters; and (5) iteratively refines and updates models and source locations by continued analysis of new events.

In the absence of Martian seismic data, we computed synthetic seismograms down to a period of 1 s using full waveform techniques based on the axisymmetric spectral element method AxisSEM. Models for the interior of Mars (radial profiles of density, P- and S-wave-speed, and attenuation) have been constructed on the basis of an average Martian mantle composition and model areotherm using thermodynamic principles and mineral physics data and were used to create synthetic waveforms. Noise was added to the synthetic seismograms in order to mimic the conditions that we envisage with the data returned from the seismometer deployed by the Mars InSight lander. This noise is based on the currently most realistic noise model that considers many possible sources. In order to demonstrate the methodology, we considered

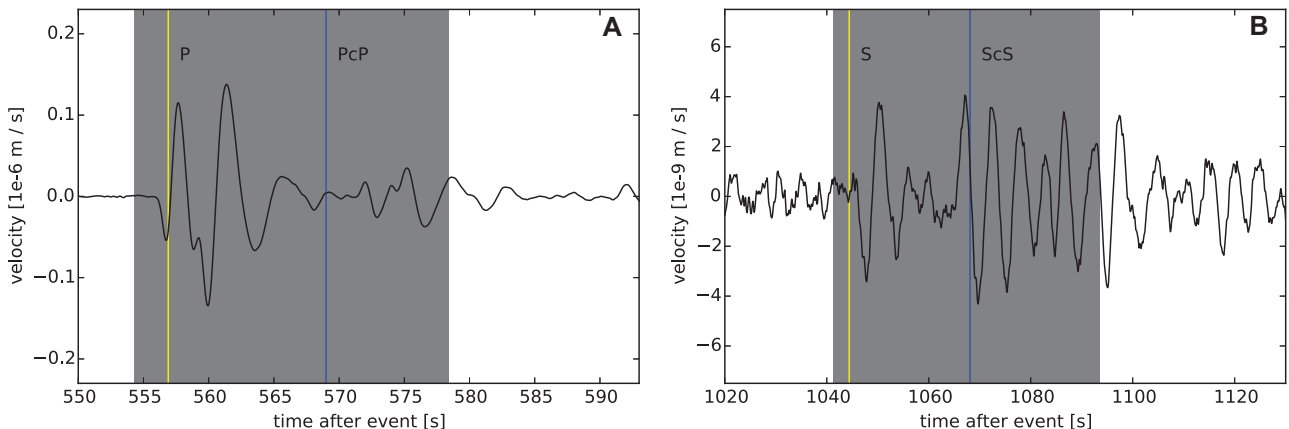


Fig. 12. Comparison of computed range of PcP (A) and ScS (B) arrival times (gray area) for all “Preliminary” inverted models with the theoretically predicted (vertical blue line) PcP arrival for model “Input” (Fig. 3). The vertical yellow line refers to the P- and S-wave arrival obtained by manual inspection of the seismogram in the “Preliminary” inversion. Traces are filtered in the frequency range 1–5 s and show vertical (A) and horizontal (B) components, respectively. (For interpretation of the references to colour in this figure caption, the reader is referred to the web version of this article.)

sources similar to those contained in a realistic Martian seismicity catalogue. These include a relatively large-sized event (M_w 5.1) at an epicentral distance of 86.6° for which both major- and minor-arc surface waves (R1, R2, and R3) and body wave arrivals are available and a smaller event (M_w 3.8) at a distance of 27.6° for which only the minor-arc surface wave (R1) and body wave arrivals are usable.

Applying our location algorithm (Böse et al., 2016) on the synthetic waveforms, we have shown that we are able to locate an event in space (epicentral distance, back azimuth, and source depth) and time to high accuracy. Epicentral distance and origin time were determined to an accuracy of $\sim 0.5-1^\circ$ and $\pm 3-6$ s, respectively, whereas source depth could be determined to an accuracy of 1–2 km (for those events where seismic depth phases could be identified). With the particular events and noise level chosen, we were able to extract information on Rayleigh-wave group velocity dispersion in the period ranges 14–48 s (M_w 5.1) and 14–34 s (M_w 3.8), respectively. Inversion of the dispersion data in combination with body-wave travel time picks allows us to determine mantle velocity structure to an uncertainty of $\leq 5\%$ for V_S and $\sim 5\%$ for V_P .

This study is based on purely radial models and complexities related to three-dimensional structure, particularly in the crust and lithosphere, will undoubtedly render the waveforms more complex than envisaged here. As discussed in more detail in Böse et al. (2016), we foresee the following complexities arise: (1) scattering – broadening of surface wave-train and decreased amplitudes at short periods; (2) crustal dichotomy – modification of Rayleigh-wave travel time; (3) Mars' ellipticity – change in travel time of Rayleigh-waves relative to a spherically symmetric model, as a result of which estimates of epicentral distance and origin time will be affected. The full extent to which these effects interfere with the present approach are currently being investigated and will be described in forthcoming analyses. However, since crustal thickness is known to within a constant factor (Neumann et al., 2004; Wieczorek and Zuber, 2004), including ellipticity corrections commonly applied in surface-wave tomography on Earth (Nolet, 2008) are expected to be applicable on Mars.

In spite of such caveats, we have demonstrated the feasibility of our single-station-single-event surface-wave-based procedure for locating marsquakes, extracting and inverting dispersion data in combination with body-wave travel times. Following this, we have shown how the inverted models can be used as a diagnostic tool to aid in locating seismic phases that might elude visual identification or otherwise be difficult to assign. While the identification of seismic phases performed here was limited to the most distinct arrivals and served to illustrate the predictive power of the method, we envision improved analysis in the future by combining with polarization and amplitude information.

In the future we will also consider aspects of interior structure interpretation. As an example, we may note the importance of a low-velocity layer in the upper mantle of Mars. If present, such a layer provides insights into the dynamics of the Martian mantle, its volatile content, and thermal evolution. The seismic signature of a low-velocity layer is distinct from that produced by models without this feature, making it potentially observable with a single seismic station (Okal and Anderson, 1978; Zheng et al., 2015). As discussed by Zheng et al. (2015), the most obvious candidates for detecting a low-velocity layer are direct body-wave arrivals (P or S), through the presence of a shadow zone and the dispersion characteristics of surface-waves. Detecting a shadow zone with a single station will nonetheless remain challenging and will depend critically on Martian seismic activity and the geographical distribution of marsquakes. In comparison, if relatively large surface-waves are excited, these will, by the methodology employed herein, provide a relatively easy tool for distinguishing models with and without

low-velocity layers through the characteristic form of the dispersion curve that these give rise to. Note that this can be done without knowledge of the location of the particular marsquake. In relation hereto, excitation of normal modes by a sufficiently large marsquake such as the one modeled in this study, will provide an independent means of inverting for structure (Lognonné et al., 1996).

Ultimately, the success of the methodology developed here for locating marsquakes and determining structural parameters, will depend crucially on the as yet unknown levels of Martian seismicity and background noise. Extracting longer period surface waves, including Love waves in addition to Rayleigh waves as well as overtones, would help in sounding deeper into the mantle, but, again, will hinge on the level of background seismic noise on Mars, installation characteristics, and Martian seismicity. These parameters will be estimated with the return of data beginning November 2018.

Acknowledgements

We would like to thank Lapo Boschi and an anonymous reviewer for comments on the manuscript. We would also like to acknowledge Francis Nimmo for sharing his visco-elastic attenuation code. This work was supported by grants from the Swiss National Science Foundation (SNF-ANR project 157133 "Seismology on Mars") and from the Swiss National Supercomputing Centre (CSCS) under project ID s528. Numerical computations have also been performed on the ETH cluster Brutus.

Appendix A. Supplementary data

Supplementary data associated with this article can be found, in the online version, at <http://dx.doi.org/10.1016/j.pepi.2016.05.017>.

References

- Al-Attar, D., Woodhouse, J.H., 2008. Calculation of seismic displacement fields in self-gravitating earth models—applications of minors vectors and symplectic structure. *Geophys. J. Int.* 175 (3), 1176–1208.
- Anderson, D.L., 1989. Theory of the Earth. Blackwell Scientific Publications.
- Anderson, D.L., Given, J.W., 1982. Absorption band q model for the earth. *J. Geophys. Res. Solid Earth* 87 (B5), 3893–3904.
- Anderson, D.L., Miller, W.F., Latham, G.V., Nakamura, Y., Toksoz, M.N., Dainty, A.M., Duennebier, F.K., Lazarewicz, A.R., Kovach, R.L., Knight, T.C.D., 1977. Seismology on Mars. *J. Geophys. Res.* 82, 4524–4546.
- Banerdt, W.B., Smrekar, S., Lognonné, P., Spohn, T., Asmar, S.W., Banfield, D., Boschi, L., Christensen, U., Dehant, V., Folkner, W., Giardini, D., Goetze, W., Golombek, M., Grott, M., Hudson, T., Johnson, C., Kargl, G., Kobayashi, N., Maki, J., Mimoun, D., Mocquet, A., Morgan, P., Panning, M., Pike, W.T., Tromp, J., van Zoest, T., Weber, R., Wieczorek, M.A., Garcia, R., Hurst, K., Mar, 2013. InSight: A Discovery Mission to Explore the Interior of Mars. In: Lunar and Planetary Science Conference. Vol. 44 of Lunar and Planetary Inst. Technical Report. p. 1915.
- Benjamin, D., Wahr, J., Ray, R.D., Egbert, G.D., Desai, S.D., 2006. Constraints on mantle anelasticity from geodetic observations, and implications for the J_2 anomaly. *Geophys. J. Int.* 165, 3–16.
- Bertka, C.M., Fei, Y., 1997. Mineralogy of the Martian interior up to core-mantle boundary pressures. *J. Geophys. Res.* 102, 5251–5264.
- Bertka, C.M., Fei, Y., 1998. Density profile of an SNC model Martian interior and the moment-of-inertia factor of Mars. *Earth Planet. Sci. Lett.* 157, 79–88.
- Bills, B.G., Neumann, G.A., Smith, D.E., Zuber, M.T., 2005. Improved estimate of tidal dissipation within Mars from MOLA observations of the shadow of Phobos. *J. Geophys. Res. (Planets)* 110, 7004.
- Böse, M., Clinton, J., Ceylan, S., Euchner, F., van Driel, M., Khan, A., Giardini, D., 2016. A Probabilistic framework for single-station location of seismicity on Earth and Mars. *Phys. Earth Planet. Sci.* in preparation.
- Chael, E.P., 1997. An automated rayleigh-wave detection algorithm. *Bull. Seismol. Soc. Am.* 87 (1), 157–163.
- Connolly, J.A.D., 2009. The geodynamic equation of state: what and how. *Geochem. Geophys. Geosyst.* 10 (10), n/a-n/a, q1001.
- Crotwell, H.P., Owens, T.J., Ritsema, J., 1999. The taup toolkit: flexible seismic travel-time and ray-path utilities. *Seismol. Res. Lett.* 70 (2), 154–160.
- Dreibus, G., Wänke, H., 1985. Mars, a volatile-rich planet. *Meteoritics* 20, 367–381.
- Durek, J.J., Ekström, G., 1996. A radial model of anelasticity consistent with long-period surface-wave attenuation. *Bull. Seismol. Soc. Am.* 86 (1A), 144–158.

- Dziewonski, A., Romanowicz, B., 2007. 1.01 – overview. In: Schubert, G. (Ed.). *Treatise on Geophysics*. Elsevier, Amsterdam, pp. 1–29.
- Dziewonski, A.M., Anderson, D.L., 1981. Preliminary reference Earth model. *Phys. Earth Planet. Inter.* 25, 297–356.
- Efroimsky, M., 2012. Tidal dissipation compared to seismic dissipation: in small bodies, Earths, and super-Earths. *Astrophys. J.* 746, 150.
- Eisermann, A.S., Ziv, A., Wust-Bloch, G.H., 2015. Real-time Back Azimuth for Earthquake Early Warning. *Bulletin of the Seismological Society of America*.
- Gagnepain-Beyneix, J., Lognonné, P., Chenet, H., Lombardi, D., Spohn, T., 2006. A seismic model of the lunar mantle and constraints on temperature and mineralogy. *Phys. Earth Planet. Inter.* 159, 140–166.
- Garcia, R.F., Gagnepain-Beyneix, J., Chevrot, S., Lognonné, P., 2011. Very preliminary reference Moon model. *Phys. Earth Planet. Inter.* 188, 96–113.
- Golombek, M.P., Banerdt, W.B., Tanaka, K.L., Tralli, D.M., 1992. A prediction of Mars seismicity from surface faulting. *Science* 258, 979–981.
- Grimm, R.E., 2013. Geophysical constraints on the lunar Procellarum KREEP Terrane. *J. Geophys. Res. (Planets)* 118, 768–778.
- Gudkova, T.V., Lognonné, P., Gagnepain-Beyneix, J., 2011. Large impacts detected by the Apollo seismometers: impactor mass and source cutoff frequency estimations. *Icarus* 211, 1049–1065.
- Jackson, I., Faul, U.H., 2010. Grainsensitive viscoelastic relaxation in olivine: towards a robust laboratory-based model for seismological application. *Phys. Earth Planet. Inter.* 183, 151–163.
- Karato, S.-i., 2013. Geophysical constraints on the water content of the lunar mantle and its implications for the origin of the Moon. *Earth Planet. Sci. Lett.* 384, 144–153.
- Kawamura, T., Kobayashi, N., Tanaka, S., Lognonné, P., 2015. Lunar Surface Gravimeter as a lunar seismometer: investigation of a new source of seismic information on the Moon. *J. Geophys. Res. (Planets)* 120, 343–358.
- Khan, A., Connolly, J.A.D., 2008. Constraining the composition and thermal state of Mars from inversion of geophysical data. *J. Geophys. Res. (Planets)* 113, 7003.
- Khan, A., Connolly, J.A.D., Pommier, A., Noir, J., 2014. Geophysical evidence for melt in the deep lunar interior and implications for lunar evolution. *J. Geophys. Res. (Planets)* 119, 2197–2221.
- Khan, A., Mosegaard, K., 2002. An inquiry into the lunar interior: a nonlinear inversion of the Apollo lunar seismic data. *J. Geophys. Res. (Planets)* 107, 5036.
- Khan, A., Mosegaard, K., Williams, J.G., Lognonné, P., 2004. Does the Moon possess a molten core? Probing the deep lunar interior using results from LLR and Lunar Prospector. *J. Geophys. Res. (Planets)* 109, 9007.
- Khan, A., Pommier, A., Neumann, G., Mosegaard, K., 2013. The lunar moho and the internal structure of the moon: a geophysical perspective. *Tectonophysics* 609, 331–352, moho: 100 years after Andrija Mohorovičić.
- Knapmeyer, M., 2004. Tbbox: a matlab toolbox for the computation of 1d teleseismic travel times. *Seismol. Res. Lett.* 75 (6), 726–733.
- Knapmeyer, M., Oberst, J., Hauber, E., Wählisch, M., Deuchler, C., Wagner, R., 2006. Working models for spatial distribution and level of Mars' seismicity. *J. Geophys. Res. E Planets* 111 (11), 1–23.
- Knapmeyer, M., Weber, R.C., 2015. Seismicity and interior structure of the moon. In: Tong, V.C.H., Garcia, R.A. (Eds.). *Extraterrestrial Seismology*. Cambridge University Press, Cambridge, pp. 203–225.
- Kuskov, O.L., Panferov, A.B., 1993. Thermodynamic models for the structure of the martian upper mantle. *Geochem. Int.* 30, 132.
- Lainey, V., Dehant, V., Pätzold, M., 2007. First numerical ephemerides of the Martian moons. *Astron. Astrophys.* 465, 1075–1084.
- Larmat, C., Montagner, J.-P., Capdeville, Y., Banerdt, W.B., Lognonné, P., Vilotte, J.-P., 2008. Numerical assessment of the effects of topography and crustal thickness on martian seismograms using a coupled modal solution spectral element method. *Icarus* 196, 78–89.
- Lognonné, P., Banerdt, W.B., Giardini, D., Christensen, U., Mimoun, D., de Raucourt, S., Spiga, A., Garcia, R., Mocquet, A., Panning, M., Beucler, E., Boschi, L., Goetz, W., Pike, T., Johnson, C., Weber, R., Wieczorek, M., Larmat, K., Kobayashi, N., Tromp, J., Mar, 2012. Insight and single-station broadband seismology: from signal and noise to interior structure determination. In: *Lunar and Planetary Science Conference*, vol. 43 of *Lunar and Planetary Inst. Technical Report*. p. 1983.
- Lognonné, P., Beyneix, J.G., Banerdt, W.B., Cacho, S., Karczewski, J.F., Morand, M., 1996. Ultra broad band seismology on InterMarsNet. *Planets Space Sci.* 44, 1237.
- Lognonné, P., Gagnepain-Beyneix, J., Chenet, H., 2003. A new seismic model of the Moon: implications for structure, thermal evolution and formation of the Moon. *Earth Planet. Sci. Lett.* 211, 27–44.
- Lognonné, P., Johnson, C., 2007. 10.03 – planetary seismology. In: Schubert, G. (Ed.). *Treatise on Geophysics*. Elsevier, Amsterdam, pp. 69–122.
- Lognonné, P., Mosser, B., 1993. Planetary seismology. *Surv. Geophys.* 14, 239–302.
- Lognonné, P., Pike, T.W., 2015. Planetary seismometry. In: Tong, V.C.H., Garcia, R.A. (Eds.). *Extraterrestrial Seismology*. Cambridge University Press, Cambridge, pp. 91–106.
- Longhi, J., Knittle, E., Holloway, J.R., Wänke, H., 1992. The bulk composition, mineralogy and internal structure of Mars. In: Kieffer, H.H., Jakosky, B.M., Snyder, C.W., Matthews, M.S. (Eds.). *Mars*. Univ. of Arizona Press, pp. 184–208.
- Lyubetskaya, T., Korenaga, J., 2007. Chemical composition of Earth's primitive mantle and its variance: 1. method and results. *J. Geophys. Res. Solid Earth* 112 (B3), n/a–n/a, b0321.
- McDonough, W.S., Sun, S., 1995. The composition of the earth. *Chem. Geol.* 120 (34), 223–253, *Chemical Evolution of the Mantle*.
- McSween Jr., H.Y., 1994. What we have learned about Mars from SNC meteorites. *Meteoritics* 29, 757–779.
- Mimoun, D., Lognonné, P., Banerdt, W.B., Hurst, K., Deraucourt, S., Gagnepain-Beyneix, J., Pike, T., Calcutt, S., Bierwirth, M., Roll, R., Zweifel, P., Mance, D., Robert, O., Nébut, T., Tillier, S., Lauden, P., Kerjean, L., Perez, R., Giardini, D., Christensen, U., Garcia, R., Mar, 2012. The InSight SEIS experiment. In: *Lunar and Planetary Science Conference*, vol. 43 of *Lunar and Planetary Inst. Technical Report*. p. 1493.
- Minster, J.B., Anderson, D.L., 1981. A model of dislocation-controlled rheology for the mantle. *R. Soc. B* 299 (1449), 319–356.
- Mocquet, A., Vacher, P., Grasset, O., Sotin, C., 1996. Theoretical seismic models of Mars: the importance of the iron content of the mantle. *Planets Space Sci.* 44, 1251–1268.
- Mosegaard, K., Tarantola, A., 1995. Monte carlo sampling of solutions to inverse problems. *J. Geophys. Res.: Solid Earth* (1978–2012) 100 (B7), 12431–12447.
- Murdoch, M., Minoun, D., Lognonné, P.H., SEIS science team, 2015a. Seis performance model environment document. Tech. rep., ISGH-SEIS-JF-ISAE-030.
- Murdoch, M., Minoun, D., Lognonné, P.H., SEIS science team, 2015b. Seis performance budgets. Tech. rep., ISGH-SEIS-JF-ISAE-0010.
- Nakamura, Y., 1983. Seismic velocity structure of the lunar mantle. *J. Geophys. Res.* 88, 677–686.
- Nakamura, Y., 2015. *Planetary seismology: early observational results*. In: Tong, V.C. H., Garcia, R.A. (Eds.). *Extraterrestrial Seismology*. Cambridge University Press, Cambridge, pp. 91–106.
- Neumann, G.A., Zuber, M.T., Wieczorek, M.A., McGovern, P.J., Lemoine, F.G., Smith, D.E., 2004. Crustal structure of Mars from gravity and topography. *J. Geophys. Res.: Planets* 109 (E8), e08002.
- Nimmo, F., Faul, U.H., 2013. Dissipation at tidal and seismic frequencies in a melt-free, anhydrous Mars. *J. Geophys. Res. (Planets)* 118, 2558–2569.
- Nimmo, F., Faul, U.H., Garnero, E.J., 2012. Dissipation at tidal and seismic frequencies in a melt-free Moon. *J. Geophys. Res. (Planets)* 117, 9005.
- Nissen-Meyer, T., van Driel, M., Stähler, S.C., Hosseini, K., Hempel, S., Auer, L., Colombi, A., Fournier, A., 2014. AxiSEM: broadband 3-D seismic wavefields in axisymmetric media. *Solid Earth* 5 (1), 425–445.
- Nolet, G., 2008. *A Breviary of Seismic Tomography*. Cambridge University Press, Cambridge, UK.
- Okan, E.A., Anderson, D.L., 1978. Theoretical models for Mars and their seismic properties. *Icarus* 33, 514–528.
- Panning, M.P., Beucler, E., Drilleau, M., Mocquet, A., Lognonné, P., Banerdt, W.B., 2015. Verifying single-station seismic approaches using Earth-based data: preparation for data return from the InSight mission to Mars. *Icarus* 248, 230–242.
- Peterson, J., 1993. Observations and modeling of seismic background noise. *Tech. Rep. Open-File Report 93-322*, US Geological Survey, Albuquerque, New Mexico.
- Phillips, R., 1991. Expected rate of marsquakes. In: *Scientific Rationale and Requirements for a Global Seismic Network on Mars*, vol. 91-02, LPI Technical Rep. Lunar and Planetary Institute, Houston TX, pp. 35–38.
- Pommier, A., Leinenweber, K., Tasaka, M., 2015. Experimental investigation of the electrical behavior of olivine during partial melting under pressure and application to the lunar mantle. *Earth Planet. Sci. Lett.* 425, 242–255.
- Rivoldini, A., Van Hoolst, T., Verhoeven, O., Mocquet, A., Dehant, V., 2011. Geodesy constraints on the interior structure and composition of Mars. *Icarus* 213, 451–472.
- Selby, N.D., 2001. Association of rayleigh waves using backazimuth measurements: application to test ban verification. *Bull. Seismol. Soc. Am.* 91 (3), 580–593.
- Smith, D.E., Zuber, M.T., Mar, 2002. The crustal thickness of Mars: accuracy and resolution. In: *Lunar and Planetary Science Conference*, vol. 33 of *Lunar and Planetary Inst. Technical Report*. p. 1893.
- Sohl, F., Schubert, G., Spohn, T., 2005. Geophysical constraints on the composition and structure of the Martian interior. *J. Geophys. Res. (Planets)* 110, 12008.
- Stixrude, L., Lithgow-Bertelloni, C., 2005a. Thermodynamics of mantle minerals – I. Physical properties. *Geophys. J. Int.* 162, 610–632.
- Stixrude, L., Lithgow-Bertelloni, C., 2011. Thermodynamics of mantle minerals – II. Phase equilibria. *Geophys. J. Int.* 184, 1180–1213.
- Taylor, G.J., 2013. The bulk composition of Mars. *Chem. Erde/Geochem.* 73, 401–420.
- Teanby, N.A., Wooley, J., 2011. Seismic detection of meteorite impacts on Mars. *Phys. Earth Planet. Inter.* 186, 70–80.
- Treiman, A.H., 1986. The parental magma of the Nakhla achondrite: ultrabasic volcanism on the shergottite parent body. *Geochim. Cosmochim. Acta* 50, 1061–1070.
- van Driel, M., Krischer, L., Stähler, S.C., Hosseini, K., Nissen-Meyer, T., 2015. Instaseis: instant global seismograms based on a broadband waveform database. *Solid Earth* 6 (2), 701–717.
- Van Hoolst, T., Dehant, V., Roosbeek, F., Lognonné, P., 2003. Tidally induced surface displacements, external potential variations, and gravity variations on Mars. *Icarus* 161, 281–296.
- Verhoeven, O., Rivoldini, A., Vacher, P., Mocquet, A., Choblet, G., Menyelle, M., Dehant, V., Van Hoolst, T., Sleewaegen, J., Barriot, J.-P., Lognonné, P., 2005. Interior structure of terrestrial planets: modeling Mars' mantle and its electromagnetic, geodetic, and seismic properties. *J. Geophys. Res. (Planets)* 110, 4009.
- Wang, Y., Wen, L., Weidner, D.J., 2013. Composition of Mars constrained using geophysical observations and mineral physics modeling. *Phys. Earth Planet. Inter.* 224, 68–76.
- Weber, R.C., Lin, P.-Y., Garnero, E.J., Williams, Q., Lognonné, P., 2011. Seismic detection of the lunar core. *Science* 331, 309.

- Wieczorek, M.A., Zuber, M.T., 2004. Thickness of the martian crust: improved constraints from geoid-to-topography ratios. *J. Geophys. Res.: Planets* 109 (E1), e01009.
- Williams, J.G., Boggs, D.H., 2015. Tides on the Moon: theory and determination of dissipation. *J. Geophys. Res. (Planets)* 120, 689–724.
- Williams, J.G., Boggs, D.H., Yoder, C.F., Ratcliff, J.T., Dickey, J.O., 2001. Lunar rotational dissipation in solid body and molten core. *J. Geophys. Res.* 106, 27933–27968.
- Yamada, R., Garcia, R.F., Lognonné, P., Kobayashi, N., Takeuchi, N., Nébut, T., Shiraishi, H., Calvet, M., Ganepain-Beyneix, J., 2013. On the possibility of lunar core phase detection using new seismometers for soft-landers in future lunar missions. *Planet. Space Sci.* 81, 18–31.
- Yamada, R., Matsumoto, K., Kikuchi, F., Sasaki, S., 2014. Error determination of lunar interior structure by lunar geodetic data on seismic restriction. *Phys. Earth Planet. Inter.* 231, 56–64.
- Yoder, C.F., Konopliv, A.S., Yuan, D.N., Standish, E.M., Folkner, W.M., 2003. Fluid core size of mars from detection of the solar tide. *Science* 300, 299–303.
- Zharkov, V.N., Gudkova, T.V., 1997. On the dissipative factor of the Martian interiors. *Planets Space Sci.* 45, 401–407.
- Zharkov, V.N., Gudkova, T.V., 2005. Construction of Martian interior model. *Sol. Syst. Res.* 39, 343–373.
- Zheng, Y., Nimmo, F., Lay, T., 2015. Seismological implications of a lithospheric low seismic velocity zone in mars. *Phys. Earth Planet. Inter.* 240, 132–141.